JSS Focus Issue on Novel Applications of Luminescent Optical Materials

Using DFT Methods to Study Activators in Optical Materials

Mao-Hua Du[z]

Materials Science and Technology Division, Oak Ridge, Tennessee 37831, USA

Density functional theory (DFT) calculations of various activators (ranging from transition metal ions, rare-earth ions, ns^2 ions, to self-trapped and dopant-bound excitons) in phosphors and scintillators are reviewed. As a single-particle ground-state theory, DFT calculations cannot reproduce the experimentally observed optical spectra, which involve transitions between multi-electronic states. However, DFT calculations can generally provide sufficiently accurate structural relaxation and distinguish different hybridization strengths between an activator and its ligands in different host compounds. This is important because the activator-ligand interaction often governs the trends in luminescence properties in phosphors and scintillators, which can be used to search for new materials. DFT calculations of the electronic structure of the host compound and the positions of the activator levels relative to the host band edges in scintillators are also important for finding optimal host-activator combinations for high light yields and fast scintillation response. Mn^{4+} activated red phosphors, scintillators activated by Ce^{3+}, Eu^{2+}, Tl^{+}, and excitons are shown as examples of using DFT calculations in phosphor and scintillator research.

© The Author(s) 2015. Published by ECS. This is an open access article distributed under the terms of the Creative Commons Attribution 4.0 License (CC BY, http://creativecommons.org/licenses/by/4.0/), which permits unrestricted reuse of the work in any medium, provided the original work is properly cited. [DOI: 10.1149/2.0011601jss] All rights reserved.

Manuscript received July 15, 2015. Published August 17, 2015. *This paper is part of the JSS Focus Issue on Novel Applications of Luminescent Optical Materials.*

Luminescence of materials when excited by photons or ionizing radiation is the foundation for numerous technologies, such as energy efficient lighting (fluorescent lamps and white LEDs), laser, medical imaging, and nuclear materials detection.[1–3] Efficient luminescence in semiconductors and insulators usually relies on the localization of excited electrons and holes at certain impurities, which act as luminescence centers (or activators). An activator can trap electrons and holes for efficient radiative recombination and is the essential component of a phosphor or scintillator material. The commonly used activators are typically multivalent ions, which can insert multiple electronic states inside the bandgap of the host material.[45] Good examples of the multivalent ions that can act as luminescent centers are rare-earth ions (e.g., Ce^{3+}, Eu^{2+}),[6–11] transition metal ions (e.g., Cr^{3+}, Mn^{4+}),[12–17] and ns^2 ions (ions with outer electron configuration of ns^2, such as Tl^{+}, Sn^{2+}).[18–20]

Energy efficiency is critically important for phosphors used for lighting. To suppress the energy loss through nonradiative recombination, a phosphor is excited by directly exciting activators, not the host (see Fig. 1a). The excitation energy is less than the bandgap energy of the host but is large enough to excite the activator. Since the excitation occurs locally at the activator, the chance for the excited activator to interact with nonradiative recombination centers, such as deep defects, is small. This is important for achieving high quantum efficiencies for phosphors. In scintillators used for detecting ionizing radiation, the radiation creates charge carriers in the valence and conduction bands of the host, which are subsequently trapped by activators, leading to radiative recombination (see Fig. 1b). In scintillators, a portion of the charge carriers need to travel a certain distance before being trapped by the activators, which increases the probability of carrier trapping and recombination at defects. Hence, efficient carrier transport in scintillators is important for achieving a high light yield and fast scintillation response.

There is significant interest in finding new phosphors and scintillators for various applications. For example, new efficient red phosphors with suitable emission wavelengths are highly desirable for producing warm white light from LEDs;[21–23,6,14] scintillators with improved energy resolutions are sought for gamma-ray spectroscopy.[24] Theoretical calculations can be useful for searching for new materials and optimizing existing materials. The important material properties that need to be calculated may differ for different applications. For finding new phosphors for lighting applications, it is important to be able to calculate absorption and emission wavelengths of phosphors accurately. The absorption wavelength must match the photon wavelength of the excitation source, e.g., mercury ion emission at 254 nm in fluorescence lamps, blue LED (∼450 nm) or near-UV (∼400 nm) radiation in LED lamps. The emission wavelength should match the spectral sensitivity of human eyes. For scintillators, the accurate determination of the emission wavelength is less important because the photo sensors (photo multiplying tubes or photo diodes), which detect the photons emitted by the scintillator, have wide spectral responses. It is more important to calculate the electronic structure of the host material and the activator levels relative to the valence and conduction band edges because these properties affect the light yield and the scintillation response.[4,5,25,26] The host bandgap should be small enough to allow a high light yield while large enough to accommodate activator levels. Highly dispersive valence and conduction bands are also important for enabling efficient energy transport and fast scintillation response.

A predictive theory that can accurately calculate the optical absorption and emission spectra of a given material is highly desirable for phosphor research. To accurately calculate the optical transition energies between multi-electronic states, methods based on multi-electronic wavefunctions should be used. Ab-initio embedded-cluster calculations[27,28] have been performed to study optical transitions at activators in various phosphors and scintillators, such as $Y_2O_3:Bi^{3+}$,[29,30] $CaF_2:Pr^{3+}$,[31] $SrCl_2:Yb^{2+}$,[32,33] $La_2CaB_{10}O_{19}:Ce^{3+}$,[34] $BaF_2:Tb^{3+}$.[35] In

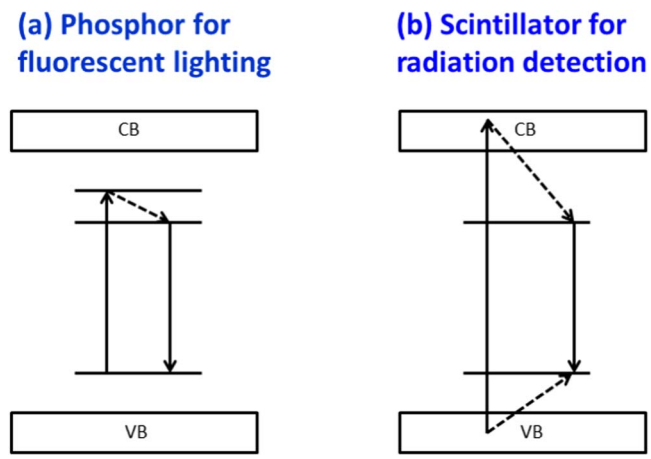

Figure 1. Schematic figures of excitation and emission in (a) a phosphor for fluorescent lighting and (b) a scintillator for radiation detection.

[z]E-mail: mhdu@ornl.gov

Downloaded on 2016-03-09 to IP 128.219.49.13 address. Redistribution subject to ECS terms of use (see ecsdl.org/site/terms_use) unless CC License in place (see abstract).

such method, a small cluster containing the activator is treated by a multi-electron quantum mechanical method. The interaction between the cluster and its surrounding ions is modeled by ab initio model potentials. The rest of the crystal environment is simulated by a large number of point charges positioned at lattice sites. Good agreement between the calculated and measured transition energies and relative oscillator strengths has been reported for various systems.[30,31,34,35] The calculation results can also assist the assignment of observed features in optical spectra to specific transitions between electronic states.

However, the state-of-the art quantum mechanical calculations still have significant errors and are too computationally demanding for practically screening a large number of potentially useful materials. The calculated and the measured transition energies differ by 0.1 eV to a few tens of eV.[30,31,34,35] An error bar of such magnitude is still significant in optical spectroscopy. For example, the emission energy near 610 nm is desirable for a red-emitting phosphor used in fluorescent lamps. The responsivity of human cone cells decreases by more than 60% when going from 610 nm to 650 nm and nearly diminishes at 700 nm. 650 nm and 700 nm wavelengths differ from 610 nm by 0.125 eV and 0.262 eV, respectively, which are in the same magnitude with the error bar of the state-of-the-art quantum mechanical calculations. Therefore, the current quantum mechanical methods based on multi-electronic wavefunctions are still limited in its predictive power when evaluating the optical properties of new phosphors.

To increase the reliability of the predictions based on computational methods, it is helpful to establish useful chemical trends and acquire deep understanding of underlying physics that governs the optical properties of materials. For example, based on the spectroscopic properties of the Mn^{4+} ion, Brik and Srivastava observed that the emission wavelength of Mn^{4+} generally increases with the increasing covalency of the Mn-ligand bonds.[36,37] Density functional theory (DFT) calculations of Mn^{4+} emission in a large number of oxides and fluorides revealed the influence of the local structures to the activator-ligand hybridization strength and the emission energies.[38,39] These insights are very useful for searching for new Mn^{4+}-activated red phosphors.

DFT[40,41] has been extensively used in computational solid state physics.[42] DFT in conjunction with local density approximation (LDA) and generalized gradient approximation (GGA) have been shown to describe many ground-state material properties very well.[43] One drawback of LDA and GGA is that they typically underestimate the band gaps of semiconductors and consequently cannot reliably predict the impurity and defect induced electronic level positions within the bandgap. Hybrid density functional methods,[44–47] which include a fraction of non-local Fock exchange, have been shown to be effective in improving the calculations of band gaps and the defect/impurity levels.[48–56]

Although DFT is a ground-state single-particle theory, the lowest excited-state can be simulated by constraining the occupancies of the DFT eigenstates. For example, the electron configurations of the excited-state Ce^{3+} and Tl^{+} can be constrained to $4f^0 5d^1$ and $6s^1 6p^1$, respectively. The absorption and emission energies, ΔE_{abs} and ΔE_{em}, are the vertical transition energies shown in Fig. 2. Following Franck-Condon principle, ΔE_{abs} is given by the total energy difference between the excited and the ground states both at the relaxed ground-state structure whereas ΔE_{abs} is calculated using the relaxed excited-state structure. The calculated ΔE_{abs} and ΔE_{em} can be compared with the experimentally observed lowest-energy absorption and emission peaks. The calculated total energy difference between the relaxed excited-state and ground-state structures can be compared with the zero phonon line in optical spectra. Such approach has been applied to the calculation of the optical transition between the ground state and the lowest excited state of Tl^{+} in NaI and Ce^{3+} in Cs_2LiYCl_6.[4,57] Good agreement (within 0.1 eV to 0.4 eV) between the results of hybrid functional calculations and the experimental results has been found.[4,55,58] Although, as a single-particle theory, DFT cannot reproduce the detailed optical absorption and emission spectra involving transitions between the ground state and many multi-electronic excited states, the calculation of the emission energy due to the transition from

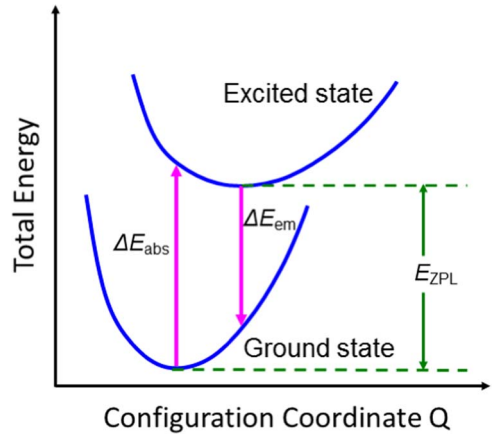

Figure 2. Schematic configuration coordinate diagram that illustrates the calculated energies of optical absorption and emission and the zero phonon line.

the lowest excited state to the ground state is still useful for phosphor research. In particular, DFT calculations can produce correct chemical trends in emission energy that can be used to assist the search for new materials.[38]

As mentioned above, for scintillator research, it is important to calculate the positions of the activator levels relative to the band edges, which determine whether a material can be activated and whether scintillation would be subject to severe thermal quenching.[25,26] Calculated electronic structures and defect properties also shed light on the efficiency of energy transport and scintillation response.[4,5] DFT is well positioned to study these issues for better understanding of scintillation mechanisms and for the search of new scintillators.

Scintillation typically involves a transition between two deep activator levels in the host bandgap, e.g., 4f and 5d levels of rare-earth ions (e.g., Ce^{3+} and Eu^{2+})[59,60] and np and ns levels of ns^2 ions (e.g., Tl^{+}),[18–20] each of which traps one type of carrier, either an electron or a hole. However, some other activators insert one level that traps one type of carrier while relying on the self-trapping of the other type of carrier. For example, Tl^{+} in CsI traps electrons on its 6p level while the hole self-traps as a V_k center, which migrates to bind with Tl^0 to form a Tl-bound exciton before radiative recombination.[55] Thus, self-trapped and dopant-bound excitons may be explored as scintillation mechanisms, which could be used in scintillators whose band gaps are too small to accommodate two activator levels. The advantage of having a smaller bandgap is the potentially larger number of radiation generated electron-hole pairs and a higher light yield. Materials with electronic structures that enhance the stability of self-trapped and dopant-bound excitons are most suited as exciton based scintillators. Hybrid density functional calculations can give good description of band gaps and charge localization associated with self-trapping. Therefore, hybrid functional calculations can be used to search small-gap scintillators with potentially high light yields activated by self-trapped or dopant-bound excitons.[61]

Note that LDA and GGA calculations typically fail to describe the localized 3d and 4f states and the charge localization in self-trapped electrons, holes, and excitons due to the self-interaction error.[62–64] The minimization of the artificial self-interaction often leads to artificial over-delocalization of orbitals. On the other hand, the Hartree-Fock (HF) calculations with exact exchange but no correlation usually overestimate the localization. Typically, band gaps and charge localization energies are overestimated by HF calculations but underestimated by LDA and GGA calculations. The hybrid density functional calculation that includes a fraction of Fock exchange gives a more balanced and more accurate description of the bandgap and the charge localization.

In this paper, DFT studies of various activators in a large number of host materials are reviewed. These include Mn^{4+} activated red phosphors as well as scintillators activated by Ce^{3+}, Eu^{2+}, Tl^{+}, self-trapped and dopant-bound excitons. The calculations reveal the

Downloaded on 2016-03-09 to IP 128.219.49.13 address. Redistribution subject to ECS terms of use (see ecsdl.org/site/terms_use) unless CC License in place (see abstract).

chemical trends that determine the emission energies and the luminescence mechanisms. New phosphors and scintillators are proposed. The insights obtained will help the search and design of more efficient phosphors and scintillators.

Mn^{4+} Activated Oxides and Fluorides

Mn^{4+} doped materials have been extensively studied for lighting,[65] holography,[66] laser,[67] and dosimetry.[68] There is a long list of Mn^{4+} activated red-emitting phosphors, including $SrTiO_3$,[69] Al_2O_3,[70] $YAlO_3$,[66] $Gd_3Ga_5O_{12}$,[71] $CaZrO_3$,[72] $Y_2Sn_2O_7$,[15] MgO,[73] K_2SiF_6,[74,75] Na_2SiF_6,[76] Na_2SnF_6,[77] and Cs_2SnF_6.[76] The Mn^{4+} activated fluoride phosphors have recently attracted considerable interest due to their potential use as red phosphors in LED devices.[73–76] However, the reactivity with water is a concern for the practical applications of fluorides in LED devices.[21] Oxides are chemically more stable than fluorides but the emission wavelengths of currently known Mn^{4+} activated oxides are too far red-shifted for general lighting. Y_2O_3:Eu^{3+} is a commercial red phosphor used in fluorescent lamps. It has an emission wavelength of 611 nm, which is ideal for human eye sensitivity. However, it is desirable to find alternative materials to rare-earth based ones for the concern of supply disruption of the rare-earth materials. Currently, the shortest Mn^{4+} emission wavelengths in fluorides and in oxides are 617 nm (Na_2SiF_6)[76] and 648 nm ($Y_2Sn_2O_7$), respectively.[15] Thus, finding a chemically stable, non-toxic Mn^{4+} activated phosphors that emit near 611 nm is of great interest to general lighting applications.

Mn^{4+} is a $3d^3$ ion. In an octahedral environment, the Mn-3d states are split into three- and two-fold degenerate t_{2g} and e_g states, respectively. The three Mn-3d electrons of Mn^{4+} exactly fill the majority-spin t_{2g} states. The crystal field splitting creates a large gap between the t_{2g} and e_g states, stabilizing the 4+ oxidation state (Fig. 3a). Therefore, Mn^{4+} is usually found on octahedral sites of solids. The emission spectrum of Mn^{4+} typically shows a sharp line corresponding to the spin- and parity-forbidden $^2E_g \rightarrow {}^4A_{2g}$ transition. This emission is nearly independent of the crystal field splitting according to the Tanabe-Sugano diagram.[78 79] However, variation of the Mn^{4+} emission energy in different hosts is still significant.[12,13] It is observed that the $^2E_g \rightarrow {}^4A_{2g}$ emission energy of Mn^{4+} is nearly linear to $\beta_1 = \sqrt{(\frac{B}{B_0})^2 + (\frac{C}{C_0})^2}$, where B and C ($B_0$ and C_0) are the Racah parameters of the Mn^{4+} ions in a crystal (free state).[12] This observation suggests that the Mn^{4+} emission energy increases with weaker Mn-ligand hybridization.Based on DFT calculations, this trend can be understood in a single-particle picture considering different Mn-ligand hybridization in the ground and the emitting states.[38] Increasing Mn-ligand distance and distorting bond angles around the Mn octahedral site both lead to weakened Mn-ligand hybridization and higher Mn^{4+} emission energies. This is an important trend, which can explain the higher $^2E_g \rightarrow {}^4A_{2g}$ emission energies of Mn^{4+} in fluorides than in oxides by recognizing the weaker Mn-ligand hybridization in fluorides.

DFT calculations with Perdew-Burke-Ernzerhof (PBE)[80] type of GGA functionals were used to study the Mn^{4+} emission in oxides and fluorides.[38,39] Many different structural forms, including perovskite, rock salt, pyrochlore, bixbyite, etc., which all have octahedral or distorted octahedral sites for Mn doping, were investigated. Since the $^2E_g \rightarrow {}^4A_{2g}$ emission involves only a spin flip, the Mn^{4+} emission energy is calculated by

$$\Delta E_{em} = E(1\mu_B) - E(3\mu_B), \quad [1]$$

where $E(1\mu_B)$ and $E(3\mu_B)$ are the total energies of structurally relaxed low-spin ($1\mu_B$) and high-spin ($3\mu_B$) states of Mn^{4+} as schematically shown in Fig. 3. ΔE_{em} calculated by Eq. 1 corresponds to the zero phonon line in optical emission spectra.

As mentioned above, DFT is a ground-state single-particle theory, which in principle is incapable of calculating the transition energy between multi-electronic states. Nevertheless, the DFT-PBE method has several advantages, i.e., (1) it provides full structural relaxation and good treatment of Mn-ligand hybridization and that (2) it is an efficient method enabling fast screening of a large number of materials. The variation of the Mn^{4+} emission energy in different hosts is caused by the different Mn-ligand hybridization strengths,[12,13] which can be distinguished by DFT calculations. Therefore, the DFT-PBE method is expected to produce a correct trend in Mn^{4+} emission energies in different hosts.

The Mn^{4+} emission energies for several oxide and fluoride hosts with known experimental data are calculated using the DFT-PBE method (Fig. 4).[38] It can be seen that PBE-calculated emission energies are significantly lower than the experimental ones. However, the emission energy trend is reproduced well by the PBE calculations except for the transition from oxides to fluorides. The lack of a jump in the calculated emission energy when transitioning from oxides to fluorides in Fig. 4 is likely due to that the self-interaction error (larger in fluorides than in oxides) in the PBE calculation makes fluorides appear more covalent, which increases the hybridization and lowers the emission energy. The Mn^{4+} emission energy trend is described very well by the DFT-PBE method if the ligands in all host materials are the same. The DFT-PBE method can better distinguish the different Mn-ligand hybridization strengths if the variation is caused by different bonding configurations rather than different electronegativities of the ligands. The variation of the Mn^{4+} emission energy is smaller in fluorides than in oxides (see Fig. 4 and Ref. 13). This is likely because the Mn-F hybridization is generally very weak and its variation in different fluorides is not significant.

Fig. 5 shows the PBE-calculated $^2E \rightarrow {}^4A_2$ emission energy of Mn^{4+} in a large number of oxides as a function of Mn-O bond length.[38,39] Pyrochlore compounds (represented by black triangles in

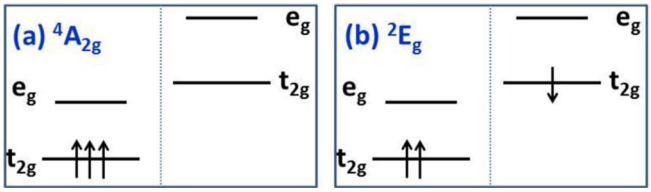

Figure 3. Single-particle schematic diagrams of (a) the $^4A_{2g}$ ground state and (b) the ^2E_g excited state of Mn^{4+} in an octahedral environment. The left and right panels in (a) and (b) show spin-up and –down levels, respectively. Note that the John-Teller splitting of the partially occupied levels in ^2E_g state is not shown.

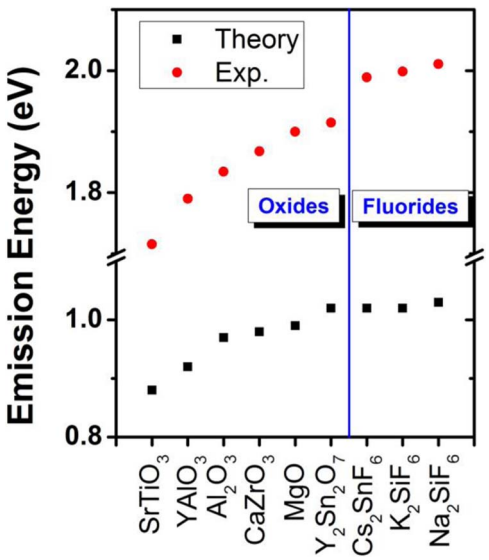

Figure 4. Experimental and theoretical values of Mn^{4+} emission energies for a number of oxides and fluorides. The theoretical values are obtained by DFT-PBE calculations (Ref. 38).

Downloaded on 2016-03-09 to IP 128.219.49.13 address. Redistribution subject to ECS terms of use (see ecsdl.org/site/terms_use) unless CC License in place (see abstract).

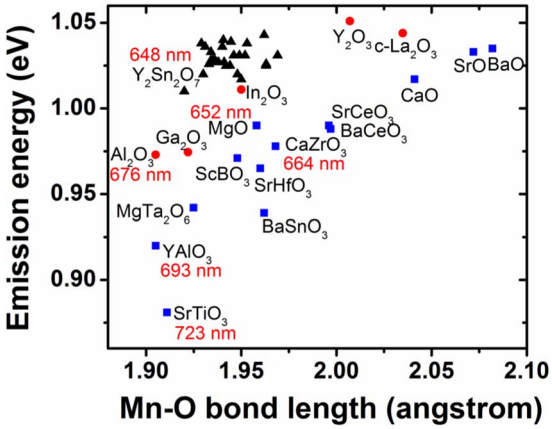

Figure 5. PBE-calculated Mn^{4+} emission energies as functions of Mn-O bond length for oxides. The Mn-O bond length is the average over the six Mn-O bond lengths in the MnO_6 octahedron. The experimental values are shown (in red) wherever available (i.e., for $SrTiO_3$, $YAlO_3$, Al_2O_3, $CaZrO_3$, MgO, and $Y_2Sn_2O_7$). Some of the materials shown in the figure have no or small (< 2°) O-Mn-O bond angle distortion (blue squares) while some other have relatively large (> 4°) O-Mn-O bond angle distortion (red circles and black triangles). Black triangles represent pyrochlore oxides which are shown in more details in Fig. 6 (Ref. 39).

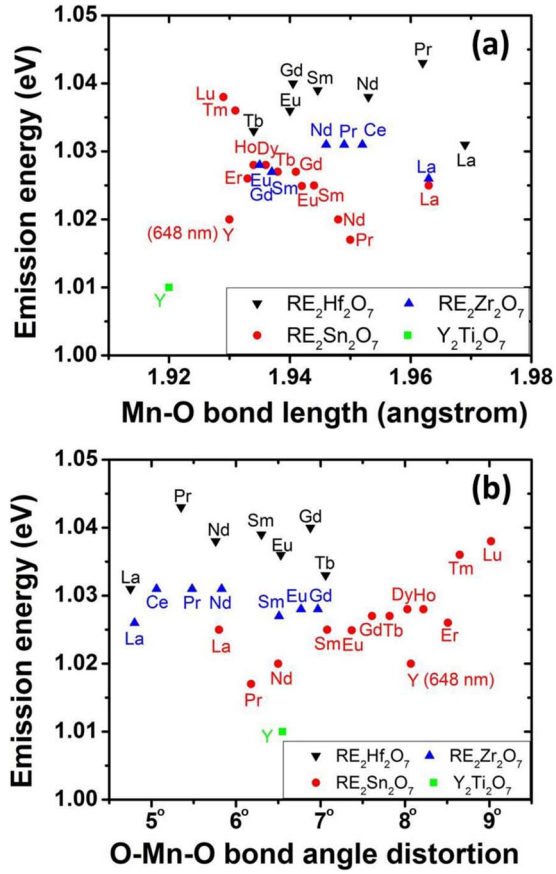

Figure 6. PBE-calculated Mn^{4+} emission energies for rare-earth pyrochlores as functions of Mn-O bond length (a) and O-Mn-O bond angle distortion (b). The calculated Mn-O bond lengths and Mn^{4+} emission energies for $Eu_2Zr_2O_7$ and $Gd_2Zr_2O_7$ are nearly the same and are therefore represented by one data point in (a) (Ref. 39).

Fig. 5) are shown in more details in Fig. 6.[39] Despite their diverse crystal structures, these materials all contain octahedral or distorted octahedral lattice sites for stabilizing Mn^{4+}. Many of these compounds have not been studied experimentally as hosts for Mn^{4+}. The calculated emission energies of Mn^{4+} in new host materials are compared with the existing ones, for which the experimental data are available. Since PBE calculations can produce a good trend of Mn^{4+} emission energies in different oxide hosts (see Fig. 4), this approach can identify new oxide host materials with emission energies, which are higher than those currently known and are closer to that of $Y_2O_3:Eu^{3+}$ (the commercial red phosphor used in fluorescent lamps). Several important observations can be made from the results in Figures 5 and 6:

(1) Many Mn^{4+}-activated oxide phosphors (e.g., Y_2O_3 and most of the pyrochlores in Fig. 6) are shown to exhibit higher emission energies than $Y_2Sn_2O_7:Mn^{4+}$, which currently has the highest experimentally measured Mn^{4+} emission energy in oxides. These emission energies, although not accurately predicted by the PBE calculations, should be closer to that of $Y_2O_3:Eu^{3+}$ than those of existing oxide phosphors.

(2) Longer Mn-O bonds generally lead to higher emission energy, or shorter wavelength, because longer Mn-O bonds usually correspond to weaker Mn-O hybridization. This trend is most evident among hosts of the same structural form. For example, this is the case for Mn^{4+} emission in oxides of perovskite (e.g., $SrTiO_3$, $BaSnO_3$, $SrHfO_3$, $CaZrO_3$, $SrCeO_3$, and $BaCeO_3$) and rock salt (i.e., MgO, CaO, SrO, BaO) structures. However, this rule is violated when comparing materials of different structural forms. For examples, the calculated Mn^{4+} emission energies of pyrochlores are generally higher than those of perovskites even if their bond lengths are not significantly different (see Fig. 5).

(3) The structural distortion of the MnO_6 octahedron affects the Mn-O hybridization. The results in Fig. 5 combined with structural analyses suggest that the Mn^{4+} emission energy increases if the O-Mn-O angle in MnO_6 octahedrons deviates from 90°. To better illustrate this trend, the materials shown in Fig. 5 are separated into several groups. The group represented by blue squares has small O-Mn-O bond angle distortions in MnO_6 octahedrons while those represented by red circles and black triangles have larger bond angle distortion. The former have either perovskite or rock-salt structures with small (<2°) or no O-Mn-O bond angle distortion, while the latter are pyrochlores or oxides of trivalent metals (i.e., Al, Ga, In, Y) with bond angle distortion larger than 4°. The O-Mn-O bond angle is 90° in cubic perovskites (e.g., $SrTiO_3$, $BaSnO_3$) and in alkali-earth metal oxides of rock-salt structures, and is only slightly distorted from 90° in orthorhombic perovskites (e.g., <2° in CaZrO3). In contrast, the deviation of the O-Mn-O bond angles from 90° is significant in pyrochlores, reaching nearly 9° in the case of $Lu_2Sn_2O_7$ for instance (see Fig. 6b). Analyses of the wavefunctions of Mn-3d states in $Y_2Sn_2O_7:Mn^{4+}$ shows that the O-Mn-O bond angle distortion forces the d_{xy}, d_{yz}, and d_{xz} orbitals of t_{2g} to move out of the MnO_4 plane. This should reduce the hybridization between the Mn-3d (t_{2g}) states and the O-2p orbitals. The weakened Mn-O hybridization in pyrochlores compared to that in perovskites explains the higher Mn^{4+} emission energies of $Y_2Ti_2O_7$, $Y_2Sn_2O_7$ and $La_2Zr_2O_7$ (pyrochlores) than those of $SrTiO_3$, $BaSnO_3$ and $CaZrO_3$ (perovskites). The O-Mn-O bond angles in Al_2O_3, Ga_2O_3, In_2O_3, and Y_2O_3 also have significant distortions from 90° (e.g., ∼9° in $Al_2O_3:Mn^{4+}$), which lead to higher Mn^{4+} emission energies. For example, due to the larger O-Mn-O bond angle distortion in Al_2O_3 (∼9°) than in perovskite $YAlO_3$ (<1°), the emission energy of $Al_2O_3:Mn^{4+}$ is significantly higher than that of $YAlO_3:Mn^{4+}$ although in both materials Mn^{4+} occupies the Al^{3+} site and the Mn-O bond lengths are nearly the same. It can be seen in Fig. 5 that, when comparing Mn^{4+} emission energies among materials with similar Mn-O bond lengths, the materials with larger O-Mn-O bond angle distortion (red circles and black triangles) generally exhibit higher emission energies than those with small bond angle distortion (blue squares).

In a $RE_2B_2O_7$ rare-earth pyrochlore, each B ion is bonded with six O ions in a distorted octahedral structure.[81] The six B-O bond lengths are equal to each other whereas the O-B-O bond angles deviate somewhat from 90°. Increasing the size of the RE^{3+} cation leads to increased B-O bond length and decreased O-B-O bond angle distortion. When a B cation is substituted by a Mn cation, the increased

Downloaded on 2016-03-09 to IP 128.219.49.13 address. Redistribution subject to ECS terms of use (see ecsdl.org/site/terms_use) unless CC License in place (see abstract).

Mn-O bond length and the decreased O-Mn-O bond angle as the result of increasing the size of the RE^{3+} cation have the opposite effects, i.e., the former weakens the Mn-O hybridization whereas the latter enhances it. This results in the lack of a clear trend in the Mn^{4+} emission energy as a function of Mn-O bond length or O-Mn-O bond angle distortion in zirconate and hafnate pyrochlores, as shown in Figures 6a and 6b.

For stannate pyrochlores, as RE^{3+} cation size decreases from La^{3+} to Lu^{3+}, Mn^{4+} emission energies exhibit a rising trend when the Mn-O bond length decreases (which enhances Mn-O hybridization) and the O-Mn-O bond angle distortion increases (which weakens Mn-O hybridization). Since the Mn^{4+} emission energy increases with weakening Mn-O hybridization, the results in Fig. 6 demonstrate that, for rare-earth stannate pyrochlores, the increase of the O-Mn-O bond angle distortion has a stronger effect on Mn-O hybridization than the decrease of the Mn-O bond length.

The results in Fig. 5 suggest that Mn^{4+} activated phosphors with weak Mn-ligand hybridization (between Mn 3d(t_{2g}) states and ligand p states) tend to exhibit higher emission energies. The weak hybridization can be caused by long Mn-ligand distance and/or distorted bond angles around the Mn octahedral site.

Several new oxide host materials (e.g., Y_2O_3, $La_2Zr_2O_7$, and BaO) are found for Mn^{4+}. Their emission energies are higher than those currently known for Mn^{4+} doped oxides and should be closer to that of Y_2O_3:Eu^{3+} (commercial red phosphor for fluorescent lighting). When Mn^{4+} is introduced as donors or acceptors (e.g., Mn^{4+} is a donor in Y_2O_3: Mn^{4+}), doping with compensating dopants is needed to stabilize the 4+ oxidation state of Mn and to ensure a large Mn^{4+} concentration. Chemical stability of phosphors in the operating and manufacturing environments is important. Alkali-earth oxides (such as BaO) react strongly to water and thus are not suitable for use in fluorescent or LED lamps.

Ce^{3+} and Eu^{2+} Activated Scintillators

Ce^{3+} and Eu^{2+} are important activators in many phosphors and scintillators, e.g., $Y_3Al_5O_{12}$:Ce^{3+} yellow phosphor,[82] Sr[$LiAl_3N_4$]:Eu^{2+} red phosphor,[23] $LaBr_3$:Ce^{3+} and SrI_2:Eu^{2+} scintillators.[24] The emission at Ce^{3+} and Eu^{2+} involves the transition of an electron from the 5d level to the 4f level (see Fig. 7). Standard DFT calculations based on LDA and GGA functionals cannot describe the highly localized 4f states correctly. For example, the partially occupied 4f shell of Ce^{3+} ion should split, giving rise to an energy gap between the occupied and unoccupied 4f states; but LDA and GGA calculations typically give a metallic solution. Therefore, LDA/GGA+U[25,26] and hybrid density functional calculations[4,5] have been used to better treat the 4f levels of Ce and Eu. However, neither LDA/GGA+U nor hybrid density functional calculations have been shown to calculate the 5d-4f emission energy sufficiently accurate for evaluating the suitability of a given phosphor for lighting applications. Most calculations have focused on Ce^{3+} and Eu^{2+} activated scintillators. One of the goals was to determine whether a material can be activated by Ce^{3+} and Eu^{2+} by examining the positions 4f and 5d levels relative to the valence band maximum (VBM) and the conduction band minimum (CBM), respectively.

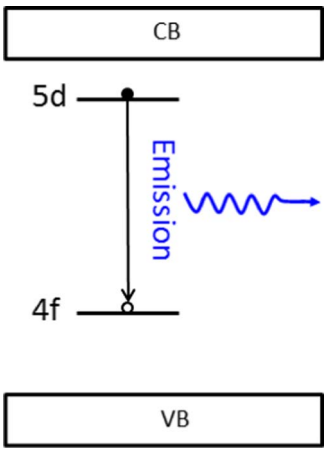

Figure 7. Schematic of 5d-4f emission at a rare earth activator.

PBE+U method was adopted to screen a large number of Ce^{3+} and Eu^{2+} doped materials (>100 new materials) for their potential as scintillators.[25,26] In the PBE+U method, effective U parameters are applied on Ce and Eu 4f levels to match the calculated 4f to host VBM gap with the experimental energy gap for some known scintillating and nonscintillating Ce and Eu doped materials. The ground states of Ce^{3+} and Eu^{2+} have the electron configuration of $4f^1 5d^0$ and $4f^7 5d^0$, respectively. For excited state calculations, the occupancies of the single-particle levels are constrained to give the electron configurations of $4f^0 5d^1$ for $(Ce^{3+})^*$ and $4f^6 5d^1$ for $(Eu^{2+})^*$. The degree of localization of the 5d wavefunctions is used as the criterion to determine whether an electron can be trapped by the 5d level, which is the prerequisite for the 5d-4f emission. A number of new Ce^{3+} and Eu^{2+} activated scintillators (e.g., Ba_2YCl_7:Ce and Ba_2CsBr_5:Eu) were suggested based on theoretical calculations and were subsequently synthesized and found to be bright scintillators.[25,26]

It is found in these PBE+U calculations of $(Ce^{3+})^*$ and $(Eu^{2+})^*$ that most of the examined materials exhibit strong overlap between the Ce/Eu 5d states and the conduction band states and that a deep 5d level does not usually exist in the host bandgap. This problem causes difficulty in determine whether the electron trapping at Ce or Eu 5d is favored. In contrast, in hybrid functional calculations, the Ce induced 5d level is clearly observed inside the bandgap when it is occupied by an electron. The partial correction of the self-interaction error in the hybrid functional calculation creates a large splitting between the occupied and the unoccupied 5d states. The calculations of Cs_2LiYCl_6:Ce using PBE0[45] hybrid functionals found a deep Ce 5d level for the excited-state $(Ce^{3+})^*$.[4]

Examining the positions of the single-particle 4f and 5d levels of Ce and Eu[25,26] is not a rigorous way to determine the energetics of electron and hole trapping at the 5d and 4f levels, respectively. Nevertheless, it is sufficient to provide an initial screening. To calculate the energetics of electron and hole trapping, one can calculate the charge transition level,[4] which is given by

$$\varepsilon(q/q') = \frac{E_{D,q'} - E_{D,q}}{q - q'}, \qquad [2]$$

where $E_{D,q}$ ($E_{D,q'}$) is the total energy of the supercell that contains the relaxed structure of a defect or dopant at charge state q (q'). If the calculated charge transition levels for both the hole trapping at the 4f level of Ce^{3+} and the subsequent electron trapping at the 5d level of Ce^{4+} are inside the host bandgap, the radiative recombination at Ce can occur. This approach has been applied to Ce doped elpasolite compounds including Cs_2LiYCl_6 and Cs_2AgYCl_6.[4,5] Calculating the electron and hole trapping energies at the activator can determine whether a material can be activated by a specific activator. The calculations of the bandgap and the band dispersion of the host compound can further give insight on the potential light yield and energy transport efficiency in a scintillator.

Elpasolites are a large family of quaternary halides[83] with a general chemical formula of $A_2BB'X_6$, where A and B are monovalent cations (such as alkali metal ions), B' is a trivalent ion (such as a rare earth ion), and X is a halogen ion (see Fig. 8). The rich chemical composition of elpasolites enables the tuning of electronegativity of the A, B, and B′ cations to modify the bandgap and the conduction band dispersion.[5] Combining the electronic structure calculations for the host and the carrier trapping energies at the activator is an effective tool to search for scintillators which have band gaps small enough for high light yield while large enough for accommodating activator levels and which have efficient energy transport for fast scintillation. However, accurately calculating the charge transition levels based on hybrid functional

Downloaded on 2016-03-09 to IP 128.219.49.13 address. Redistribution subject to ECS terms of use (see ecsdl.org/site/terms_use) unless CC License in place (see abstract).

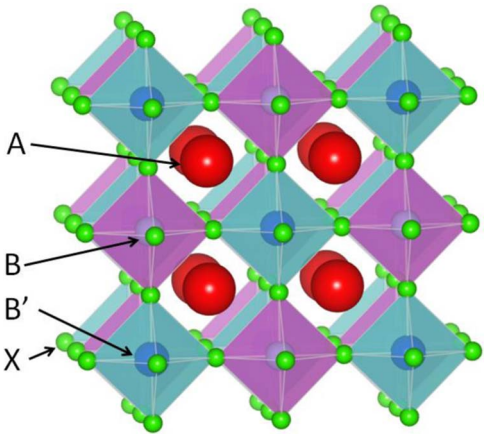

Figure 8. Structure of an elpasolite compound ($A_2BB'X_6$).

calculations is much more time consuming than using the PBE+U method.

Figure 9a shows the band structure of Cs_2LiYCl_6. The conduction band of Cs_2LiYCl_6 is made up of Y 4d states (see Figs. 9a and 9b). Replacing Li by Ag, the PBE0 calculated bandgap is reduced from 7.08 eV[4] for Cs_2LiYCl_6 to 6.08 eV[5] for Cs_2AgYCl_6. The electron and hole trapping at the 5d and the 4f levels of Ce^{3+} is energetically favored in both Cs_2LiYCl_6 and Cs_2AgYCl_6 according to the PBE0 calculations.[4,5] However, a smaller bandgap should potentially lead to a higher light yield. In the conduction band of Cs_2AgYCl_6, the Ag 5s band overlaps with the Y 4d bands (see Figs. 9c and 9d). The CBM states of Cs_2AgYCl_6 are made up of more delocalized Ag 5s states, which should enable faster electron transport than that in Cs_2LiYCl_6. This example shows that the chemical composition of elpasolites can be tuned to optimize the bandgap and the band dispersion for potentially higher light yields and faster scintillation response.

ns^2 Ions as Activators

Besides transition-metal and rare-earth ions, a number of heavy 6p (Tl, Pb, Bi) and 5p (In, Sn, Sb) ions are also important multivalent ions, which act as luminescent centers in many materials. These ions in their ground states all have the outer electronic configuration of ns^2 and are therefore called ns^2 ion. The hybridization between the ns and np states of these ions and the host states can create ns- and np-derived electronic states inside the bandgap of the host material. These gap states give rise to sub-band-gap optical transitions. Tl^+ doped NaI and CsI are two important high-performance scintillators that have been widely used for radiation detection.[2] The 6p→6s transition is responsible for the Tl emission in NaI:Tl^+.[18–20] The emission in CsI:Tl^+ appear to be related to both the hole polaron (V_k center) and the electron trapped at Tl, or Tl-bound exciton.[2,84,85]

The optical transitions between the ns and np states of a ns^2 ion are usually interpreted and modeled by using Seitz model.[86] The Seitz model is based on a two-electron picture, in which the ground state (ns^2) is a singlet $^1S_0$ state and the excited states (nsnp) consist of $^3P_0$, $^3P_1$, $^3P_2$ triplet states and a $^1P_1$ singlet state, as shown in Fig. 10. Details on the optical transitions in ns^2 ions based on the Seitz model can be found in several review articles.[18–20]

The extensions of the Seitz model based on pure ionic model,[87,88] molecular orbit (MO) theory,[89,90] and ab-initio embed cluster method[27,28] have been used to quantitatively calculate various properties related to the optical transitions (e.g., absorption and emission energies, line shapes, intensity ratio, etc.). The MO[87,88] and the ab-initio embed cluster[29,30] calculations showed results in good agreement with the spectroscopic data. DFT calculations have also been

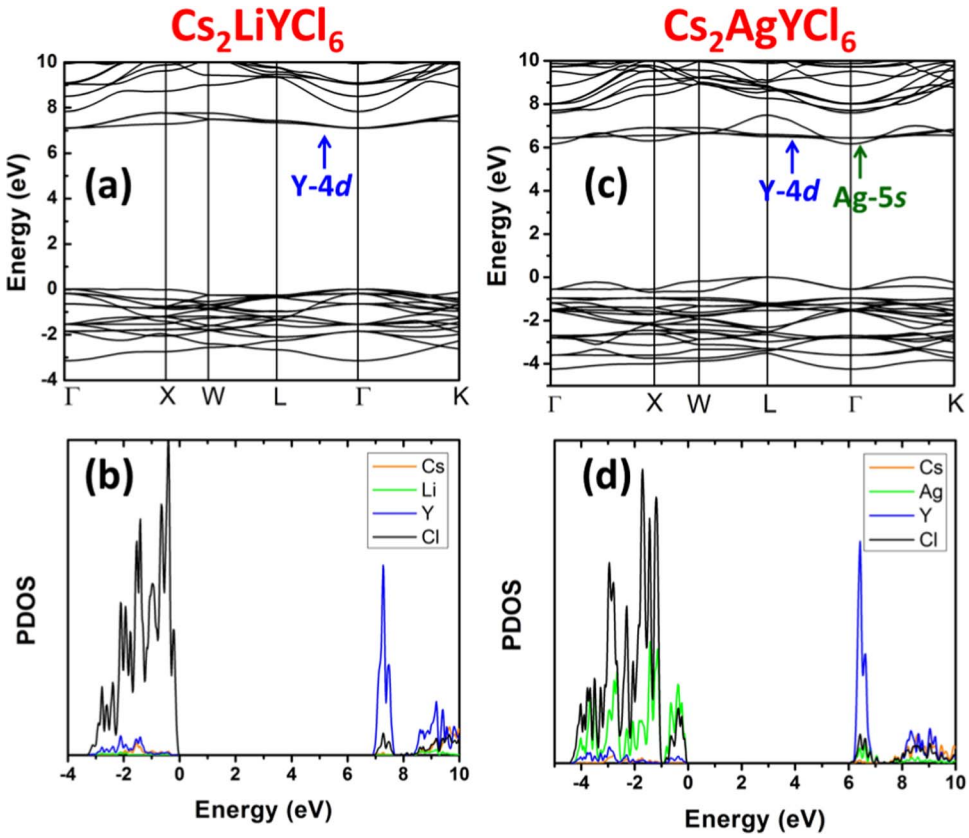

Figure 9. (a) Band structure and (b) projected density of states (PDOS) of Cs_2LiYCl_6; (c) Band structure and (d) PDOS of Cs_2AgYCl_6. The energy of the VBM is set to zero (Ref. 5).

Downloaded on 2016-03-09 to IP 128.219.49.13 address. Redistribution subject to ECS terms of use (see ecsdl.org/site/terms_use) unless CC License in place (see abstract).

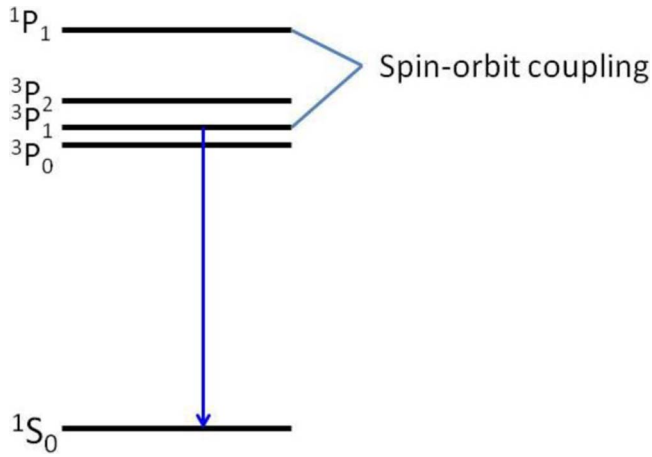

Figure 10. The ns^2 ground state and the nsnp excited state described in a two-electron picture. The spin-triplet $^3P_{0,1,2}$ states are split by the spin-orbit coupling. The $^3P_1$ state couples with the $^1P_1$ state through the spin-orbit coupling and becomes radiative as shown in the figure.

performed to study Tl^+ in alkali halides.[57] DFT as a single-particle ground-state method cannot reproduce the transitions between multi-electronic states in optical spectra. However, the calculated absorption and emission energies are in good agreement with the experimental results between the ground state and the lowest excited state.[57,58]

The advantage of DFT calculations is that it gives good description of the host band structure and provides accurate structural relaxation. Whether the specific emission between the nsnp and ns^2 states as described by the Seitz model can occur depends on the positions of the ns and np states relative the host band edges. The knowledge of the electronic structure of both the host and the activator is needed to understand the different scintillation mechanisms observed in different host materials (e.g., NaI:Tl vs. CsI:Tl). Sufficiently accurate structural relaxation is important for incorporating correct hybridization strength between the activator and its ligands in the calculations. The different hybridization strengths in different hosts determine the chemical trend of the activator-induced gap levels relative to the host bands. This is important for the understanding of the luminescence mechanisms in different hosts and for the search of new host-activator combinations with desirable scintillation properties.

Figure 11a shows the DOS for NaI:Tl calculated using the PBE functionals. The valence band is predominantly of I-5p character. Both Tl 6s and 6p states hybridize with the I-5p states. The resulting Tl-6s bonding level is below the valence band while the anti-bonding Tl-6s* level is above the VBM as shown in Fig. 11a.

The six Tl-6p* levels are split by the spin-orbit coupling to two lower- and four higher-lying levels. The two lower states are more localized and near the CBM while the four higher states have relatively stronger mixing with the host conduction band states. Hybrid functional calculations show that the lowest Tl-6p* single-particle level is slightly above the CBM by 0.29 eV for Tl^+. Upon trapping a hole, the empty Tl-6p* level remains above the CBM for Tl^{2+}. However, the lowest Tl-6p* level of Tl^{2+}, once occupied, descends below the CBM to stabilize the electron trap, $Tl^{+,*}$.

The optical absorption energy is calculated following the Franck-Condon principle. The energy difference between the $Tl^{+,*}$ (Tl 6s6p) excited state and the Tl^+ (Tl $6s^2$) ground state calculated using the Tl^+ ground-state structure is 4.06 eV,[57] reasonably close to the experimentally observed A-band absorption energy of 4.35 eV.[2] The emission energies calculated by taking the energy difference between the ground-state structure and the tetragonally and trigonally distorted excited-state structures are 3.89 eV[57] and 2.85 eV,[58] close to the experimentally observed emission energies of 3.76 eV and 2.95 eV,[2] respectively.

The Tl-I bond length increases from NaI, KI, RbI, CsI (rocksalt), to CsI (simple cubic) as shown in Table I, which corresponds to weaker Tl-I hybridization. From Figs. 11a to 11d, the Tl-6s* level gradually merge with the valence band and the energy separation between the Tl-6s bonding and Tl-6s* antibonding states decreases when the Tl-I bond length increases (weaker hybridization).

CsI has a different crystal structure [simple cubic (SC) CsCl structure] than that of the other alkali metal iodides [rocksalt (RS) NaCl structure]. As a result of the further reduced Tl-I hybridization in CsI:Tl due to longer Tl-I bonds (see Table I), the Tl-6s* state resonates with the valence band and disappears from the bandgap, as shown in Fig. 10e. The weak Tl-I hybridization in CsI also lowers the Tl-6p* level, which resides deep inside the bandgap. This is in contrast to NaI:Tl, KI:Tl, and RbI:Tl, where the Tl-6p* level is near the CBM.

The Tl-I bond lengths and the I-I distances are shown in Table I for NaI, KI, RbI, and CsI (SC). CsI (SC) has the longest Tl-I bond length and a relatively short I-I distance close to that of NaI. Therefore, CsI (SC) has the weakest Tl-I hybridization and a relatively wide valence band among the alkali halides studied in this work. These explains the disappearance of the Tl-6s* level from the CsI bandgap.

The unique electronic structure for CsI:Tl determines that the luminescence mechanism for CsI is different from that of many other alkali halides. The emission from Tl-activated alkali halides is typically of the type of Tl 6p*→6s* transition. But the emission from the CsI:Tl is shown to be involved with the self-trapped hole or the V_k center.[2,82,83] The hybrid functional calculations show that the electron trapping at the Tl-6p* level ($Tl^+ + e^- \rightarrow Tl^0$) and the hole self-trapping at a V_k center lower the total energy by 1.4 and 0.6 eV, respectively.

Electron paramagnetic resonance experiments showed that the rate of formation of the V_k centers is increased orders of magnitudes by the Tl doping in some alkali halides due to electron trapping by Tl^+.[91] The V_k center can migrate and binds with Tl^0.[82] The emission from CsI:Tl is likely due to Tl-bound excitons.[83]

For Tl-doped bromides and chlorides, the valence band is lower, narrower, and closer to the Tl-6s level, compared to Tl-doped iodides. In KCl:Tl^+, the hybridization between the Tl-6s state and the Cl 3p states is more confined within the nearest-neighbor halogen ions to Tl. The anti-bonding Tl-6s* state is more localized in Tl-doped chlorides than in iodides because the Cl 3p states are more localized than the I 5p states (narrower valence band). The DOS for KCl:Tl^+ shows a deep Tl-6s* level inside the bandgap (Fig. 11f).

The results above show that both the hybridization strength between the Tl and its ligands and the ionicity of the host material have strong impact on the positions of the Tl-induced electronic states relative to the band edges. The Tl 6s level is typically below the valence band while the Tl 6p levels are above the valence band.[92,93] The Tl-halogen hybridization (mainly within the nearest neighbors) produces two antibonding levels, i.e., Tl-6s* and −6p* levels, as schematically shown in Fig. 12. Strong/weak Tl-halogen hybridization should result in high/lowTl-6s* and Tl-6p* levels relative to the band edges. Hybridization among halogen ions is also important. For instance, strong halogen-halogen hybridization widens the valence band and lower the positions of the Tl-6s* and Tl-6p* levels relative to the VBM. The interplay of the Tl-halogen and halogen-halogen hybridization determines the positions of the Tl-6s* and −6p* levels relative to the band edges.[57]

A combination of the strong Tl-halogen and weak halogen-halogen hybridization could result in the scenario depicted in Fig. 12a, where both Tl-6s* and −6p* levels are inside the bandgap and act as hole and electron traps, respectively, leading to radiative recombination. On the other hand, weak Tl-halogen hybridization combined with strong halogen-halogen hybridization may lead to the scenario depicted in Fig. 12b, where only the Tl-6p* level is inside the bandgap to trap electrons. Nevertheless, efficient luminescence is still possible in the scenario of Fig. 12b because the hole can be localized by a small hole polaron bound to the Tl^0 electron trap, leading to efficient radiative recombination. The emissions in NaI:Tl and CsI:Tl can be categorized into the scenarios depicted in Figs. 12a and 12b, respectively.

Downloaded on 2016-03-09 to IP 128.219.49.13 address. Redistribution subject to ECS terms of use (see ecsdl.org/site/terms_use) unless CC License in place (see abstract).

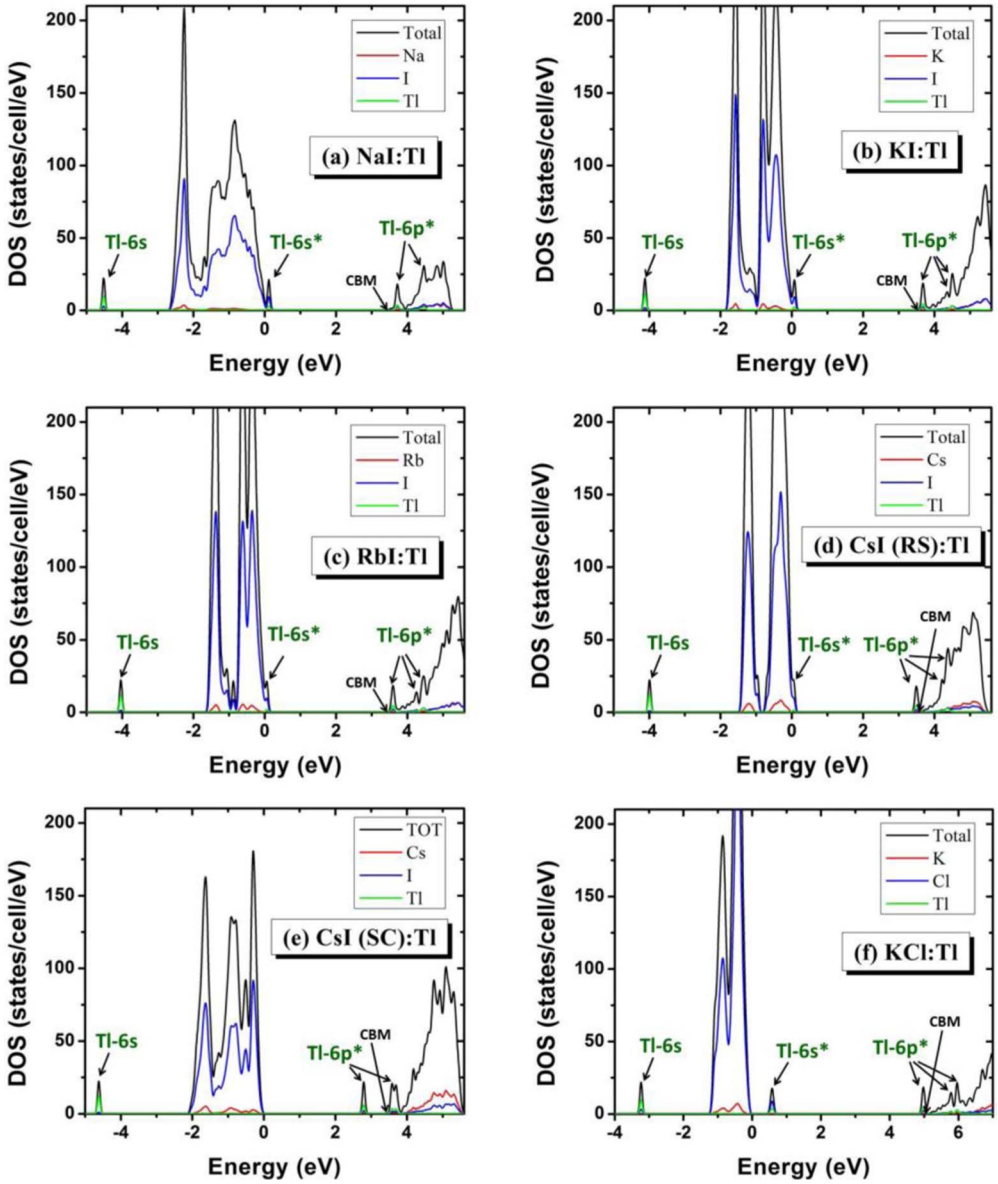

Figure 11. Density of states (DOS) for Tl doped (a) NaI, (b) KI, (c) RbI, (d) CsI (rocksalt), (e) CsI (simple cubic), and (f) KCl. The energy of VBM is set at zero. Note that the band gaps are underestimated due to the use of PBE functionals (Ref. 57).

Among many ns^2 ions that are activators in halide scintillators, such as In^+, Ga^+, Tl^+, Ge^{2+}, Sn^{2+}, Pb^{2+}, and Bi^{3+},[19] Tl^+ appears to be most efficient. Others often suffers from slow scintillation decay, strong afterglow, or low quantum yield.[2,94,95] Pb^{2+} and Bi^{3+} are the heaviest ions among the ns^2 ions, enabling strong spin-orbit coupling and more efficient $^3P_1 \rightarrow {}^1S_0$ emission. But a large energy separation between the lowest excited state $^3P_0$ and the $^3P_1$ states can also result from the strong spin-orbit splitting and reduce the electron population on the radiative $^3P_1$ state.[92]

Table I. The calculated Tl-I bond lengths and the nearest-neighbor I-I distances, in NaI:Tl, KI:Tl, RbI:Tl, CsI:Tl. Tl_{Cs} in simple-cubic (SC) CsI undergoes a structural distortion. The Tl-I bond length shown for CsI (SC) is the average over all Tl-I bonds.

	NaI	KI	RbI	CsI (SC)
Tl-I bond length (Å)	3.37	3.55	3.63	3.93
I-I distance (Å)	4.57	5.02	5.24	4.60

Many experiments on Pb and Bi activated phosphors and scintillators involve fluoride or oxide-based large-band-gap host materials,[92,93,96–99] which have narrow valence band width and low VBM.[100] This may lead to the electronic structure depicted in Fig. 12a and the emission consistent with the Seitz model, i.e., the $6p^* \rightarrow 6s^*$ emission. It is possible that the $6p^* \rightarrow 6s^*$ transition at Pb^{2+} and Bi^{3+} is not efficient due to reasons such as the large energy separation between the $^3P_0$ and $^3P_1$ levels. However, the efficiency of the $6p^* \rightarrow V_k$ type of emission has not been studied in Pb^{2+} and Bi^{3+} activated materials. Since the efficiency of the $6p^* \rightarrow V_k$ emission is reasonably good in CsI:Tl, it should be of interest to explore ways to activate the same emission mechanism in Pb^{2+}, Bi^{3+}, and other ns^2-ion activated materials. The key to activate such emission mechanism is to have weak activator-anion hybridization and strong anion-anion hybridization as is the case for CsI:Tl. The weak activator-anion hybridization is particularly important for removing the ns^* level from the bandgap. This requires the size of the native cation to be large relative to that of the activator ion. For scintillators, a short nearest-neighbor anion-anion distance is also important for fast hole transport toward activators, which enables fast scintillation.

Downloaded on 2016-03-09 to IP 128.219.49.13 address. Redistribution subject to ECS terms of use (see ecsdl.org/site/terms_use) unless CC License in place (see abstract).

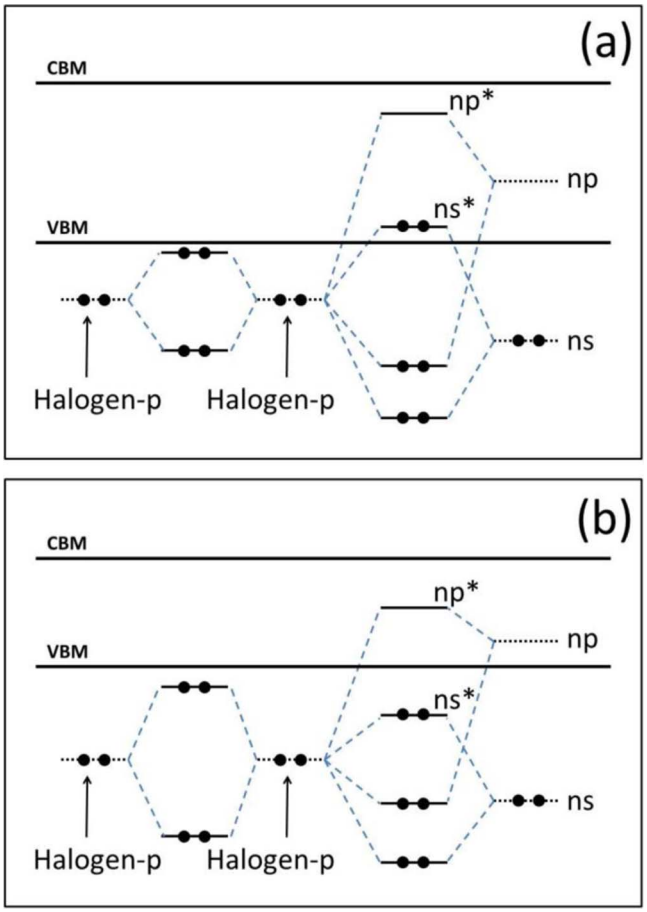

Figure 12. Schematic diagram of hybridization between the ns^2 and the halogen ions. In (a), the hybridization between the ns^2 and the halogen ion is relatively strong while the hybridization between the halogen-p states is relatively weak. In (b), the hybridization between the ns^2 and the halogen ion is relatively weak while the hybridization between the halogen-p states is relatively strong (Ref. 57).

The light yield of some of the current state-of-the-art scintillators is already close to their respective theoretical limits, which suggests that improving crystal quality may have only limited upside potential on the light yield. Further reducing the bandgap should in principle lead to higher light yield. However, a small bandgap may not be able to accommodate both the electron- and hole-trapping levels of the activator, such as the case for LaI_3:Ce.[25,101] Therefore, exploring the $np^* \rightarrow V_k$ emission in ns^2-ion activated small-band-gap materials should be of interest for searching high-light-yield scintillators and phosphors because only the electron trapping level (np^*) of the activator is required to be inside the bandgap.

Self-Trapped and Dopant-Bound Excitons as Activators

The light yield is one of the most important measures of scintillator performance. A higher light yield can potentially lead to better energy resolution of a scintillator.[2] The light yield, which is typically measured in terms of the number of photons per MeV of radiation energy, is given by

$$L = \frac{SQ}{\beta E_g} \times 10^6 \text{photons/MeV}, \quad [3]$$

where E_g is the bandgap expressed in eV, Q is the quantum efficiency of the activator, S is the energy transfer efficiency to luminescent centers or activators, which are typically found in scintillators. βE_g is the energy needed to create an electron-hole pair. β reflects the fact that only a fraction of the radiation energy is used to excite electron-hole pairs. The rest is lost to phonons. β is typically higher in covalent materials (3 to 4) than in ionic materials (1.5 to 2.0) due to the more efficient energy transfer to phonons in covalent materials.[2]

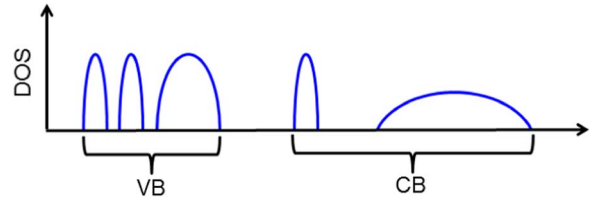

Figure 13. A schematic figure of density of states for discrete energy bands in a multinary compound semiconductor.

For several high-light-yield scintillators, such as SrI_2, their light yields are already close to their theoretical limits. For example, a light yield of 120000 photons/MeV has been reported for SrI_2.[102] If one takes the ideal conditions, i.e., $SQ = 1$ and $\beta = 1.5$ in Eq. 3, and uses the 5.2-eV bandgap calculated using the GW method,[103] one gets ~128000 photons/MeV, only slightly higher than the highest reported light yield of SrI_2. Therefore, to further increase the light yield, one has to look for materials with smaller band gaps.

Scintillators are usually insulators with large band gaps. The use of lower-gap materials as scintillators have several challenges, e.g., (1) the bandgap is too small to accommodate activator levels, which are needed to trap both electrons and holes;[104] (2) β in Eq. 1 tends to increase with decreasing bandgap.[2] These two problems have largely prevented the practical use of many semiconductors as scintillators.

To counter the above two problems and achieve high light yields in low-gap materials, one may consider materials with a small bandgap and narrow and discrete bands as schematically shown in Fig. 13. The narrow valence and conduction bands favor the charge localization and may lead to the formation of self-trapped and dopant-bound excitons, which are stable at room temperature. This may result in exciton emission at room temperature. The large energy gaps that split the valence and conduction bands may cause hot carrier luminescence and suppress the hot carrier thermalization. The reduce hot carrier thermalization may lead to enhanced impact ionization and more efficient carrier multiplication. These processes should increase the light yield.

The electronic structure shown in Fig. 13 may be realized in multinary compound semiconductors with large electronegativity difference between either cations or anions for the following reasons. In a multinary compound semiconductor, the electronic states of different cations (anions) mix to form conduction (valence) bands. The lower part of the conduction (valence) band is made up of the electronic states derived from more electronegative cations (anions) while the higher part of the conduction (valence) band is made up of those from less electronegative cations (anions). In principle, the conduction or valence band can even be split (as schematically shown in Fig. 13) if there is a large electronegativity difference between different types of cations or anions. Also, in a compound with multiple types of cations (anions), the nearest-neighbor distance in a cation (anion) sublattice can be much longer than that in a binary compound. This should lead to narrower electronic bands, further increasing the energy gaps between the separated conduction or valence bands.

Elpasolites (see Fig. 8 for the structure) exhibit narrow valence and conduction bands and many of them have conduction and valence bands split as found by DFT calculations (see Figs 9 and 14 for examples).[4,5,61] Other examples of similar electronic structures found in elpasolites can be found in Ref. 61. The PBE0 bandgap of $Cs_2NaInBr_6$ is 3.84 eV.

Fig. 14 shows the band structure of $Cs_2NaInBr_6$ calculated using PBE0 functionals.[61] The PBE0 bandgap of $Cs_2NaInBr_6$ is 3.84 eV. The DOS of $Cs_2NaInBr_6$ shows that the conduction and valence bands are both split due to the large electronegativity difference between In (1.78) and Cs/Na (0.79/0.93). The conduction band is split with a giant energy gap. The lower conduction band is a narrow band of only 1.4 eV

Downloaded on 2016-03-09 to IP 128.219.49.13 address. Redistribution subject to ECS terms of use (see ecsdl.org/site/terms_use) unless CC License in place (see abstract).

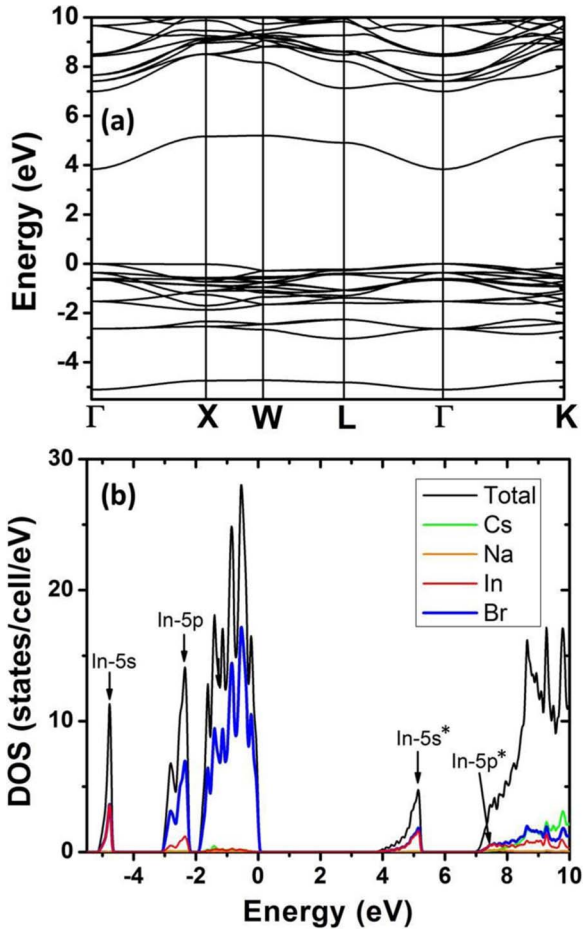

Figure 14. (a) Band structure and (b) projected density of states (DOS) of $Cs_2NaInBr_6$ calculated using PBE0 functionals. The main In-related bands are labeled in (b) according to the orbital character of In states (5s or 5p) and the bonding character [bonding or antibonding (antibonding states are labeled with an asterisk)] (Ref. 61).

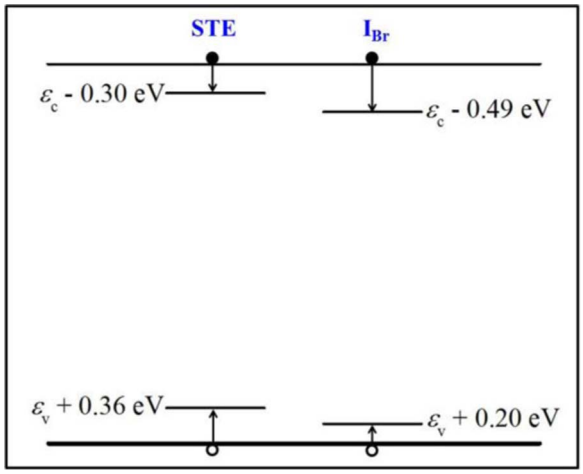

Figure 15. The hole and electron trapping levels at a STE and at an I_{Br} in $Cs_2NaInBr_6$: the hole self-trapping level ($\varepsilon(+/0) = \varepsilon_v + 0.36$ eV) and the hole trapping level at I_{Br} ($\varepsilon(+/0) = \varepsilon_v + 0.20$ eV); the electron trapping level at a small hole polaron ($\varepsilon(+/0^*) = \varepsilon_c - 0.30$ eV) and at an I_{Br}^+($\varepsilon(+/0^*) = \varepsilon_c - 0.49$ eV) (Ref. 61).

in width. It is made up of In-5s states hybridized with Br-4p states. The higher conduction band is a wider band with In-5p and Cs/Na states. The In-5s derived conduction band is separated from the Br-4p-derived valence band and the In-5p and Cs/Na dominated higher conduction band by large energy gaps, appearing almost like an isolated impurity band. The narrowness of the In-5s-derived conduction band should be due to the long In-In nearest-neighbor distance (7.85 Å) and the resulting weak In-In hybridization. The valence band of $Cs_2NaInBr_6$ is also split. The narrow bands around −5 eV and −3 eV in Fig. 14b are mainly made up of Br-4p states hybridized with In-5s and In-5p states, respectively. The higher valence band is only about 2 eV in width.

The low CBM in $Cs_2NaInBr_6$ cannot accommodate the Ce 5d levels within the band gap; therefore, $Cs_2NaInBr_6$ cannot be activated by Ce^{3+}. However, the very narrow conduction and valence bands of $Cs_2NaInBr_6$ (as shown in Fig. 14) can stabilize STEs even at room temperature because narrow bands enhance charge localization.[105] A hole in $Cs_2NaInBr_6$ can self-trap to form a V_k center with hole binding energy of 0.36 eV, which is large enough to make a hole polaron stable at room temperature (see Fig. 15). Further trapping of a free electron at the In ion adjacent to the V_k center lowers the total energy by 0.3 eV, resulting in a STE that is stable at room temperature. The total binding energy of a STE relative to a free electron and a free hole is calculated to be 0.67 eV.

The STE emission energy is calculated to be 1.39 eV, which is the total energy difference between the STE and the ground state both at the STE structure. The large calculated STE binding energy suggests that STE emission in $Cs_2NaInBr_6$ should be strong even at room temperature. The room temperature STE emission in both undoped and Ce doped Cs_2LiYCl_6 has been reported.[106,107] Note that the calculated bandgap of $Cs_2NaInBr_6$ (3.84 eV) is much smaller than that of Cs_2LiYCl_6 (7.08 eV). The large STE binding energy in such a low-gap material as $Cs_2NaInBr_6$ should be caused by the narrow discrete conduction band that promotes the electron localization.

Since a free electron can be strongly bound to a small hole polaron, it should also be bound to other localized hole centers. One can introduce a dopant to facilitate the formation of an acceptor-like bound exciton. For example, iodine can be doped into $Cs_2NaInBr_6$ to trap holes. A hole can be trapped at an I-induced level with a binding energy of 0.20 eV (Fig. 15). A free electron can further bind with I_{Br}^+ and become localized with a binding energy of 0.49 eV (Fig. 15). The trapping of a free hole and a free electron at I_{Br} forms an I_{Br}-bound exciton and lowers the total energy by 0.69 eV. The I-bound exciton emission energy is calculated to be 2.53 eV (490 nm). This is compared to 1.39 eV (893 nm) calculated for a STE. The 490 nm emission wavelength is close to that of CsI:Tl (530 nm).[108] The emission band width of the I_{Br}-bound excitons is expected to be narrower than that of the STEs due to smaller structural distortion and hence less phonon involvement.[61] The scintillation decay time for I_{Br}-bound excitons may be shorter than that for STEs since the stronger spin-orbit coupling due to the heavy iodine ions mixes the spin-triplet and -singlet states and thus promotes fast light emission.

The stability of self-trapped and dopant-bound excitons and the emission wavelength can be tuned by alloying (e.g., $Cs_2NaInBr_{6-x}Cl_x$). For example, increasing the Cl concentration in $Cs_2NaInBr_{6-x}Cl_x$ should increase the ionicity of the material and enhance charge localization, leading to more stable excitons. Also, the bandgap should increase with the Cl concentration, thereby, shortening the exciton emission wavelength and reducing the number of excitons created by radiation. Thus, alloying may be used for reducing thermal quenching of exciton emission and for tuning the exciton emission wavelength to better couple with the sensitivity of the photodetector. However, the light yield may be reduced if the bandgap is increased by alloying.

The narrow discrete conduction and valence bands not only promote exciton-based luminescence at room temperature, but also create phonon bottlenecks (electronic energy gaps much larger than phonon energies), which prevent efficient transfer of energy from hot carriers to phonons.[109–111] If hot carrier thermalization is slowed, other competing processes, such as impact ionization (which is usually considered inefficient in bulk semiconductors due to fast carrier thermalization in continuous energy bands), may take place more efficiently. Taking

Downloaded on 2016-03-09 to IP 128.219.49.13 address. Redistribution subject to ECS terms of use (see ecsdl.org/site/terms_use) unless CC License in place (see abstract).

$Cs_2NaInBr_6$ as an example, a hole in the narrow band that is more than 4 eV below the VBM (see Fig. 14a) can relax to the VBM. The released energy can be transferred to an electron in the valence band, promoting it to the conduction band (which requires energy more than the bandgap energy of 3.84 eV). The energy and momentum conservation can be satisfied in this process. The reduced hot carrier thermalization and the enhanced impact ionization should lower β in Eq. 3, leading to higher light yield.

In $Cs_2NaInBr_6$, the lower conduction band is derived from In-5s states and the higher conduction band has a significant In-5p component (see Fig. 3b). This may lead to In 5p→5s emission (inter-conduction-band luminescence). Such hot carrier luminescence can also contribute to the total light yield.

Conclusions

DFT calculations of various types of activators, i.e., Mn^{4+}, Ce^{3+}, Eu^{2+}, Tl^{+}, self-trapped and dopant-bound excitons, in phosphors and scintillators are reviewed. DFT calculations give good description of structural relaxation and activator-ligand hybridization, which reveal the chemical trends that govern luminescence properties. The established chemical trends are used for the search and the design of new materials.

PBE calculations show that Mn^{4+} activated phosphors with weak Mn-ligand hybridization tend to exhibit higher emission energies. The weak hybridization can be caused by long Mn-ligand distance and/or distorted bond angles around the Mn octahedral site. Several new oxide host materials (e.g., Y_2O_3 and $La_2Zr_2O_7$) are found for Mn^{4+}. Their emission energies are higher than those currently known for Mn^{4+} doped oxides and should be closer to that of Y_2O_3:Eu^{3+} (commercial red phosphor for fluorescent lighting). The trends of the Mn^{4+} emission energy observed can be used for searching for new Mn^{4+} activated red phosphors.

The positions of the 4f and 5d levels of Ce^{3+} and Eu^{2+} relative to their host band edges are determined using PBE+U calculations. These results are used to examine whether the electrons and holes can be trapped by Ce^{3+} and Eu^{2+}, which is a prerequisite for scintillation. New Ce^{3+} and Eu^{2+} activated materials have been proposed based on calculations and have subsequently been synthesized and found to be bright scintillators. PBE0 hybrid functional calculations are used to rigorously calculate the electron and hole trapping energies at the 5d and the 4f levels of Ce^{3+} in elpasolites, which, in combination of the electronic structure calculations of host compounds, are used to search new materials which have band gaps small enough for high light yield while large enough for accommodating the activator levels and which have large band dispersion for efficient energy transport.

DFT calculations of a series of Tl activated alkali halides, i.e., NaI, KI, RbI, and CsI, reveal that the hybridization strength between the ns^2 ion and its ligands and the ionicity of the host material both play important role in determining the scintillation mechanism ($6p^* \rightarrow 6s^*$ or $6p^* \rightarrow V_k$ emission) in ns^2 ion activated scintillators. This insight can be useful for the search and design of new combinations of the host material and the ns^2 ion, which exhibit efficient $6p^* \rightarrow V_k$ emission. The $6p^* \rightarrow V_k$ emission requires the activator to insert only one level in the host bandgap, which is useful for designing low-gap scintillators with high light yields.

PBE0 hybrid functional calculations show that the conduction and valence bands of a multinary semiconductor/insulator can be split to narrow discrete bands by a combination of large electronegativity difference among cations or anions and large nearest-neighbor distances in cation or anion sublattices. Based on calculated polaron and exciton binding energies for $Cs_2NaInBr_6$, it is found that the narrow conduction and valence bands promote the self-trapping of electrons and holes, which enhances the stabilization of self-trapped and dopant-bound excitons at room temperature. The exceptional stability of excitons provides an approach to activate exciton-based room-temperature light emission for low-gap scintillators. Furthermore, discrete bands with large energy separations (large phonon bottlenecks) in a scintillator should further suppress the hot carrier thermalization and may lead to more efficient impact ionization and higher light yield.

Although DFT cannot predict the transitions between multi-electronic states in optical spectra, it can be efficiently applied to a large number of materials to obtain trends and insights that are useful for the search of new materials. DFT calculations of various activators (ranging from transition metal ions, rare-earth ions, ns^2 ions, to self-trapped and dopant-bound excitons) shown in this paper demonstrate that DFT is a powerful tool in phosphor and scintillator research.

Acknowledgments

Work on phosphors was supported by the Critical Materials Institute, an Energy Innovation Hub funded by the U.S. Department of Energy, Office of Energy Efficiency and Renewable Energy, Advanced Manufacturing Office, while work on scintillators was supported by the U. S. Department of Energy, Office of Science, Basic Energy Sciences, Materials Sciences and Engineering Division.

References

1. G. Blasse and B. C. Grabmaier, "Luminescent Materials", Springer-Verlag, Berlin (1994).
2. Piotr A Rodnyi, "Physical Processes in inorganic scintillators", CRC Press, Boca Raton (1997).
3. J. B. Birks, "The theory and practice of scintillation counting", Pergamon Press Ltd. (1964).
4. K. Biswas and M. -H. Du, *Phys. Rev. B*, **86**, 014102 (2012).
5. M. -H. Du and K. Biswas, *J. Lumin.* **143**, 710 (2013).
6. A. A. Setlur, R. J. Lyons, J. E. Murphy, N. P. Kumar, and M. S. Kishore, *ECS J. Solid State Sci. Tech.* **2**, R3059 (2013).
7. M. D. Birowosuto and P. Dorenbos, *Phys. Stat. Sol. A*, **206**, 9 (2009).
8. P. Dorenbos, *J. Lumin.*, **91**, 91 (2000).
9. P. Dorenbos, *J. Lumin.*, **104**, 239 (2003).
10. N. J. Cherepy, S. A. Payne, S. J. Asztalos, G. Hull, J. D. Kuntz, T. Niedermayr, S. Pimputkar, J. J. Roberts, R. D. Sanner, T. M. Tillotson, E. van Loef, C. M. Wilson, K. S. Shah, U. N. Roy, R. Hawrami, A. Burger, L. A. Boatner, W. -S. Choong, and W. W. Moses, *IEEE Trans. Nucl. Sci.*, **56**, 873 (2009).
11. W. W. Moses, *Nucl. Instrum. Met. Phys. Res. A*, **487**, 123 (2002).
12. M. G. Brik, S. J. Camardello, and A. M. Srivastava, *ECS J. Solid State Sci. Tech.*, **4**, R39 (2015).
13. M. G. Brik and A. M. Srivastava, *J. Lumin.* **133**, 69 (2013).
14. J. McKittrick, M. E. Hannah, A. Piquette, J. K. Han, J. I. Choi, M. Anc, M. Galvez, H. Lugauer, J. B. Talbot, and K. C. Mishra, *ECS J. Solid State Sci. Tech.* **2**, R3119 (2013).
15. M. G. Brik and A. M. Srivastava, *Opt. Mater.* **35**, 1776 (2013).
16. S. Geschwind, P. Kisliuk, M. P. Klein, J. P. Remeika, and D. L. Wood, *Phys. Rev.*, **126**, 1684 (1962).
17. M. A. Noginov, G. B. Loutts, N. Noginova, S. Hurling, and S. Kück, *Phys. Rev. B*, **61**, 1884 (2000).
18. P. W. M. Jacobs, *J. Phys. Chem. Sol.*, **52**, 35 (1991).
19. A. Ranfagni, D. Mugnai, M. Bacci, G. Viliani, and M. P. Fontana, *Adv. Phys.*, **32**, 823 (1983).
20. W. Beall Fowler, "Physics of color centers", edited by W. Beall Fowler, Academic Press Inc., New York (1968).
21. J. Meyer and F. Tappe, *Adv. Opt. Mater.*, **3**, 424 (2015).
22. H. Zhu, C. C. Lin, W. Luo, S. Shu, Z. Liu, Y. Liu, J. Kong, E. Ma, Y. Cao, R. -S. Liu, and X. Chen, *Nat. Commun.*, **5**, 4312 (2014).
23. P. Pust, V. Weiler, C. Hecht, A. Tücks, A. S. Wochnik, A. -K. Henβ, D. Wiechert, C. Scheu, P. J. Schmidt, and W. Schnick, *Nat. Mater.*, **13**, 891 (2014).
24. M. Nikl and A. Yoshikawa, *Adv. Opt. Mater.*, **3**, 463 (2015).
25. A. Canning, A. Chaudhry, R. Boutchko, and N. Grønbech-Jensen, *Phys. Rev. B*, **83**, 125115 (2011).
26. A. Chaudhry, R. Boutchko, S. Chourou, G. Zhang, N. Grønbech-Jensen, and A. Canning, *Phys. Rev. B*, **89**, 155105 (2014).
27. Z. Barandiarán and L. Seijo, *J. Chem. Phys.*, **89**, 5739 (1988).
28. L. Seijo, Z. Barandiarán, and E. Harguindey, *J. Chem. Phys.*, **114**, 118 (2001).
29. F. Réal, V. Vallet, J. -P. Flament, and J. Schamps, *J. Chem. Phys.*, **127**, 104705 (2007).
30. F. Réal, B. Ordejón, V. Vallet, J. -P. Flament, and J. Schamps, *J. Chem. Phys.*, **131**, 194501 (2009).
31. M. Krośnicki, A. Kedziorski, L. Seijo, and Z. Barandiarán, *J. Phys. Chem. A*, **118**, 358 (2014).
32. G. Sánchez-Sanz, L. Seijo, and Z. Barandiarán, *J. Chem. Phys.*, **133**, 114506 (2009).
33. G. Sánchez-Sanz, L. Seijo, and Z. Barandiarán, *J. Chem. Phys.*, **133**, 114509 (2009).
34. L. Ning, Z. Wang, Y. Wang, J. Liu, S. Huang, C. Duan, Y. Zhang, and H. Liang, *J. Phys. Chem. C*, **117**, 15241 (2013).
35. J. L. Pascual, Z. Barandiarán, and L. Seijo, *J. Lumin.*, **145**, 808 (2014).
36. M. G. Brik and A. M. Srivastava, *J. Lumin.*, **133**, 69 (2013).

Downloaded on 2016-03-09 to IP 128.219.49.13 address. Redistribution subject to ECS terms of use (see ecsdl.org/site/terms_use) unless CC License in place (see abstract).

37. M. G. Brik, S. J. Camardello, and A. M. Srivastava, *ECS J. Solid State Sci. Tech.*, **4**, R39 (2015).
38. M. H. Du, *J. Mater. Chem. C*, **2**, 2475 (2014).
39. M. H. Du, *J. Lumin.*, **157**, 69 (2015).
40. H. Hohenberg and W. Kohn, *Phys. Rev.*, **136**, 864B (1964).
41. W. Kohn and L. J. Sham, *Phys. Rev.*, **140**, 1133A (1965).
42. M. C. Payne, M. P. Teter, D. C. Allen, T. A. Arias, and J. D. Joannopoulos, *Rev. Mod. Phys.*, **64**, 1045 (1992).
43. R. O. Jones and O. Gunnarsson, *Rev. Mod. Phys.*, **61**, 689 (1989).
44. A. D. Becke, *J. Chem. Phys.*, **98**, 1372 (1993).
45. J. P. Perdew, M. Ernzerhof, and K. Burke, *J. Chem. Phys.*, **105**, 9982 (1996).
46. H. Heyd, G. E. Scuseria, and M. Ernzerhof, *J. Chem. Phys.*, **118**, 8207 (2003).
47. J. Heyd, G. E. Scuseria, and M. Ernzerhof, *J. Chem. Phys.*, **125**, 224106 (2006).
48. J. Paier, M. Marsman, K. Hummer, G. Kresse, I. C. Gerber, and J. G. Angyan, *J. Chem. Phys.*, **124**, 154709 (2006).
49. D. Muñoz Ramo, A. L. Shluger, J. L. Gavartin, and G. Bersuker, *Phys. Rev. Lett.*, **99**, 155504 (2007).
50. D. Muñoz Ramo, J. L. Gavartin, A. L. Shluger, and G. Bersuker, *Phys. Rev. B*, **75**, 205336 (2007).
51. A. Alkauskas, P. Broqvist, and A. Pasquarello, *Phys. Rev. Lett.*, **101**, 046405 (2008).
52. A. Alkauskas, P. Broqvist, F. Devynck, and A. Pasquarello, *Phys. Rev. Lett.*, **101**, 106802 (2008).
53. M. H. Du and S. B. Zhang, *Phys. Rev. B*, **80**, 115217 (2009).
54. A. Janotti, J. B. Varley, P. Rinke, N. Umezawa, G. Kresse, and C. G. Van de Walle, *Phys. Rev. B*, **81**, 085212 (2010).
55. K. Biswas and M. H. Du, *Appl. Phys. Lett.*, **98**, 181913 (2011).
56. H. -P. Komsa, P. Broqvist, and A. Pasquarello, *Phys. Rev. B*, **81**, 205118 (2010).
57. M. H. Du, *J. Mater. Chem. C*, **2**, 4784 (2014).
58. R. Adhikari, Q. Li, R. T. Williams, A. Burger, and K. Biswas, *J. Appl. Phys.*, **116**, 223703 (2014).
59. P. Dorenbos, Scintillation mechanisms in Ce^{3+} doped halide scintillators, *phys. stat. sol. (a)*, **202**, 195 (2005).
60. M. D. Birowosuto and P. Dorenbos, Novel γ- and X-ray scintillator research: on the emission wavelength, light yield and time response of Ce^{3+} doped halide scintillators, *phys. stat. sol. (a)*, **206**, 9 (2009).
61. H. Shi and M. H. Du, *Phys. Rev. Appl.*, **3**, 054005 (2015).
62. J. L. Gavartin, P. V. Sushko, and A. L. Shluger, *Phys. Rev. B*, **67**, 035108 (2003).
63. R. Dovesi, R. Orlando, C. Roetti, C. Pisani, and V. R. Saunders, *phys. stat. sol. (b)*, **217**, 63 (2000).
64. E. A. Kotomin, R. I. Eglitis, A. V. Postnikov, G. Borstel, and N. E. Christensen, *Phys. Rev. B*, **60**, 1 (1999).
65. A. A. Setlur, E. V. Radkov, C. S. Henderson, J. -H. Her, A. M. Srivastava, N. Karkada, M. S. Kishore, N. P. Kumar, D. Aesram, A. Deshpande, B. Kolodin, L. S. Grigorov, and U. Happek, *Chem. Mater.*, **22**, 4076 (2010).
66. G. B. Loutts, M. Warren, L. Taylor, R. R. Rakhimov, H. R. Ries, G. Miller III, M. A. Curley, N. Noginova, N. Kukhtarev, H. J. Caulfield, and P. Venkateswarlu, *Phys. Rev. B*, **57**, 3706 (1998).
67. Ya Zhydachevskii, D. Galanciak, S. Kobyakov, M. Berkowski, A. Kamińska, A. Suchocki, Ya Zakharko, and A. Durygin, *J. Phys.: Condens. Matter*, **18**, 11385 (2006).
68. Ya Zhydachevskii, A. Durygin, A. Suchocki, A. Matkovskii, D. Sugak, P. Bilski, and S. Warchol, *Nucl. Instrum. Methods B*, **227**, 545 (2005).
69. Z. Bryknar, V. Trepakov, Z. Potucek, and L. Jastrabik, *J. Lumin.*, **87**, 605 (2000).
70. S. Geschwind, P. Kisliuk, M. P. Klein, J. P. Remeika, and D. L. Wood, *Phys. Rev.*, **126**, 1684 (1962).
71. A. Brenier, A. Suchocki, C. Pedrini, G. Boulon, and C. Madej, *Phys. Rev. B*, **46**, 3219 (1992).
72. M. G. Brik and A. M. Srivastava, *ECS J. Sol. State Sci. Tech.*, **2** R148 (2013).
73. K. Dunphy and W. W. Duley, *J. Phys. Chem. Solids*, **51**, 1077 (1990).
74. T. Takahashi and S. Adachi, *J. Electrochem. Soc.*, **155**, E183 (2008).
75. T. Arai and S. Adachi, *Jp. J. Appl. Phys.*, **50**, 092401 (2011).
76. Y. K. Xu and S. Adachi, *J. Appl. Phys.*, **105**, 013525 (2009).
77. Y. Arai and S. Adachi, *J. Lumin.*, **131**, 2652 (2011).
78. Y. Tanabe and S. Sugano, *J. Phys. Soc. Jp.*, **9**, 766 (1954).
79. Y. Tanabe and S. Sugano, *J. Phys. Soc. Jp.*, **11**, 864 (1956).
80. J. P. Perdew, K. Burke, and M. Ernzerhof, *Phys. Rev. Lett.*, **77**, 3865, (1996).
81. J. M. Farmer, L. A. Boatner, B. C. Chakoumakos, M. H. Du, M. J. Lance, C. J. Rawn, and J. C. Bryan, *J. Alloys Comp.*, **605**, 63 (2014).
82. Y. Shimizu, K. Sakano, Y. Noguchi, and T. Moriguchi, U.S. Pat. #5,998,925 (1999).
83. G. Meyer, *Prog. Solid State Chem.*, **14**, 141 (1982).
84. R. Gwin and R. B. Murray, *Phys. Rev.*, **131**, 508 (1963).
85. J-M Spaeth, W. Meise, and K. S. Song, *J. Phys. Condens. Matter*, **6**, 3999 (1994).
86. F. Seitz, *J. Chem. Phys.*, **6**, 150 (1938).
87. F. E. Williams, *J. Chem. Phys.* **19**, 457 (1951).
88. R. S. Knox and D. L. Dexter, *Phys. Rev.*, **104**, 1245 (1956).
89. S. Sugano, *J. Chem. Phys.*, **36**, 122 (1962).
90. D. Bramanti, M. Mancini, and A. Ranfagni, *Phys. Rev. B*, **3**, 3 (1971).
91. C. J. Delbecq, W. Hayes, and P. H. Yuster, *Phys. Rev.*, **121**, 1043 (1961).
92. M.-H. Du and D. J. Singh, *Phys. Rev. B*, **81**, 144114 (2010).
93. M.-H. Du and D. J. Singh, *Phys. Rev. B*, **82**, 045203 (2010).
94. K. P. Oboth, F. J. Lohmeier, and F. Fischer, *Phys. stat. sol. (b)*, **154**, 789 (1989).
95. J. Pejchal, E. Mihokova, M. Nikl, A. Novoselov, and A. Yoshikawa, *Opt. Mater.*, **31**, 1673 (2009).
96. H. F. Folkert, M. A. Hamstra, and G. Blasse, *Chem. Phys. Lett.*, **135**, 246 (1995).
97. I. Nicoara, M. Paraschiva, M. Stef, and F. Stef, *Eur. Phys. J. B*, **85**, 292 (2012).
98. L. K. Aminov, S. I. Nikitin, N. I. Silkin, A. A. Shakhov, R. V. Yusupov, R. Yu. Abdulsabirov, and S. L. Korableva, *J. Phys.: Conden. Matter*, **18**, 4985 (2006).
99. S. B. S. Sastry and S. M. M. Kennedy, *phys. stat. sol. (a)*, **155**, 263 (1996).
100. M.-H. Du and D. J. Singh, *J. Appl. Phys.*, **112**, 123516 (2012).
101. A. Bessiere, P. Dorenbos, C. van Eijk, K. Kramer, H. Gudel, C. Donega, and A. Meijerink, *Nucl. Instrum. Methods Phys. Res. A*, **537**, 22 (2005).
102. E. V. van Loef, C. M. Wilson, N. J. Cherepy, G. Hull, S. A. Payne, W.-S. Choong, W. W. Moses, and K. S. Shah, Crystal growth and scintillation properties of Strontium Iodide scintillators, *IEEE Trans. Nucl. Sci.*, **56**, 869 (2009).
103. P. Erhart, A. Schleife, B. Sadigh, and D. Åberg, Quasiparticle spectra, absorption spectra, and excitonic properties of NaI and SrI_2 from many-body perturbation theory, *Phys. Rev. B*, **89**, 075132 (2014).
104. A. Bessiere, P. Dorenbos, C. W. E. van Eijk, K. W. Kramer, H. U. Gudel, C. D. Donega, and A. Meijerink, *Nucl. Instrum. Meth. Phys. Res. A*, **537**, 22 (2005).
105. Y. Toyozawa, "Electrons, holes, and excitons in deformable lattice", in *Relaxation of Elementary Excitations*, Springer Series in Solid State Sci. Vol. 18, pp 3, Ed. By R. Kubo and E. Hanamura (Springer, Berlin, Heidelberg, 1980).
106. C. M. Combes, P. Dorenbos, C. W. E. van Eijk, K. W. Krämer, and H. U. Güdel, Optical and scintillation properties of pure and Ce^{3+}-doped Cs_2LiYCl_6 and Li_3YCl_6: Ce^{3+} crystals, *J. Lumin.*, **82**, 299 (1999).
107. A. Bessière, P. Dorenbos, C. W. E. van Eijk, L. Pidol, K. W. Krämer, and H. U. Güdel, Spectroscopy and anomalous emission of Ce doped elpasolite Cs_2LiYCl_6, *J. Phys.: Condens. Matter*, **16**, 1887 (2004).
108. B. C. Grabmaier, Crystal Scintillators, *IEEE Transactions on Nuclear Science*, **31**, 372 (1984).
109. U. Bockelmann and G. Bastard, Phonon scattering and energy relaxation in two-, one-, and zero-dimensional electron gases, *Phys. Rev. B*, **42**, 8947 (1990).
110. H. Benisty, C. M. Sotomayor-Terrès, and C. Weisbuch, Intrinsic mechanism for the poor luminescence properties of quantum-box systems, *Phys. Rev. B*, **44**, 10945 (1991).
111. H. T. Jiang and J. Singh, Radiative and non-radiative inter-subband transition in self assembled quantum dots, *Physica E*, **2**, 720 (1998).

Downloaded on 2016-03-09 to IP **128.219.49.13** address. Redistribution subject to ECS terms of use (see **ecsdl.org/site/terms_use**) unless CC License in place (see abstract).